Chemical Science

ROYAL SOCIETY OF CHEMISTRY

EDGE ARTICLE

View Article Online
View Journal | View Issue

Cite this: *Chem. Sci.*, 2025, **16**, 2265

All publication charges for this article have been paid for by the Royal Society of Chemistry

Received 16th October 2024
Accepted 19th December 2024

DOI: 10.1039/d4sc07031c

rsc.li/chemical-science

Single-isomer bis(pyrrolidino)fullerenes as electron-transporting materials for tin halide perovskite solar cells†

Tomoya Nakamura, *[a] Takabumi Nagai,[b] Yuki Miyake,[a] Takumi Yamada,[a] Makoto Miura,[c] Hiroyuki Yoshida,[cd] Yoshihiko Kanemitsu,[a] Minh Anh Truong,[a] Richard Murdey[a] and Atsushi Wakamiya *[a]

Although fullerene bisadducts are promising electron-transporting materials for tin halide perovskite solar cells, they are generally synthesized as a mixture of isomeric products that require a complicated separation process. Here, we introduce a phenylene-bridged bis(pyrrolidino)fullerene, **Bis-PC**, which forms only a single isomer due to geometrical restriction. When used in a tin perovskite solar cell with a $PEA_{0.15}FA_{0.85}SnI_3$ (PEA: phenylethylammonium and FA: formamidinium) light absorption layer, the resulting open-circuit voltage (V_{OC}) was 0.78 V, a value higher than that of fullerene monoadducts and comparable to that of the commonly used indene-C_{60} bisadduct (**ICBA**). The performance could be further improved by the composition engineering of perovskite, where the $PEA_{0.15}(FA_{0.87}MA_{0.13})_{0.85}SnI_3$ based device (MA: methylammonium) exhibited a photoelectric conversion efficiency of 12.3% with a V_{OC} of 0.86 V. The device with single-isomer **Bis-PC** shows superior stability to that with mixed-isomer **ICBA**, retaining its initial performance after 3000 h storage under an inert atmosphere.

Introduction

Metal halide perovskite solar cells (PSCs) are promising candidates for next-generation photovoltaics.[1–4] While solar cells based on lead (Pb) halide perovskites have achieved a power conversion efficiency (PCE) of over 26%,[5] the toxicity and environmental impact of lead are concerns for the commercialization of PSCs.[6,7] Tin (Sn) halide perovskites have emerged as one of the most promising alternatives.[8–15] They share the same crystal structures as their lead-based counterparts and have ideal bandgaps (*e.g.*, ~1.4 eV for $FASnI_3$, FA: formamidinium) for efficient single junction solar cells under AM 1.5G illumination.[16,17] Various strategies have been developed to enhance the performance of tin PSCs, including the purification of materials,[18–21] composition engineering,[22–25] and interface modification.[26,27] However, the maximum performance of Sn PSCs is still around 15%,[28,29] lower than that of their Pb counterparts.

One of the most important differences between Sn and Pb halide perovskites is the shallower valence band maximum (VBM) and conduction band minimum (CBM) energies of the Sn materials,[30] which can result in energy level mismatches with conventional charge transporting materials. For example, the LUMO energy of the commonly used electron-transporting material (ETM), C_{60} (E_{LUMO} = −4.21 eV[19]) or [6,6]-phenyl-C_{61}-butyric acid methyl ester (**PCBM**, −4.00 eV[19]), is much deeper than the CBM energy of Sn perovskite (E_{CBM} = −3.60 eV for $FASnI_3$ (ref. 23)), which may result in excessive open-circuit voltage (V_{OC}) losses. Development of ETMs with shallower LUMO energy levels is therefore desirable. An effective way to raise the LUMO energy level is to functionalize the C=C double bonds of the C_{60} cage.[31,32] Ning *et al.* reported that compared to a conventional C_{60} monoadduct, **PCBM**, an indene-C_{60} bisadduct (**ICBA**) can considerably reduce the V_{OC} loss in $PEA_{0.15}FA_{0.85}SnI_3$ (PEA: phenylethylammonium) based devices (Fig. 1a).[33] After this report, the combined use of **ICBA** and $PEA_{0.15}FA_{0.85}SnI_3$ became a trend in Sn PSC research, leading to the publication of several follow-up studies.[34–38] However, **ICBA** is a mixture of up to 18 regioisomers,[39,40] which makes the genuine relationship between the molecular structure and device performance ambiguous.

The formation of various isomers, depending on where the second addition occurs (*cis*-1 to 3, *trans*-1 to 4, *equatorial*, *etc.*) is a general challenge of the fullerene bisadducts. Isomer formation results in low yields of the desired product, which must be isolated by a time-consuming purification step.[40,41] Wei *et al.* recently reported that the number of isomers can be reduced to six in the case of a diethylmalonate-C_{60} bisadduct (**DCBA**).[42]

[a]*Institute for Chemical Research, Kyoto University, Gokasho, Uji, Kyoto 611-0011, Japan. E-mail: tomoya@scl.kyoto-u.ac.jp; wakamiya@scl.kyoto-u.ac.jp*

[b]*HARVES Co., Ltd, Saitama 330-0061, Japan*

[c]*Graduate School of Engineering, Chiba University, Chiba 263-8522, Japan*

[d]*Molecular Chirality Research Center, Chiba University, Chiba 263-8522, Japan*

† Electronic supplementary information (ESI) available. CCDC 2369060. For ESI and crystallographic data in CIF or other electronic format see DOI: https://doi.org/10.1039/d4sc07031c

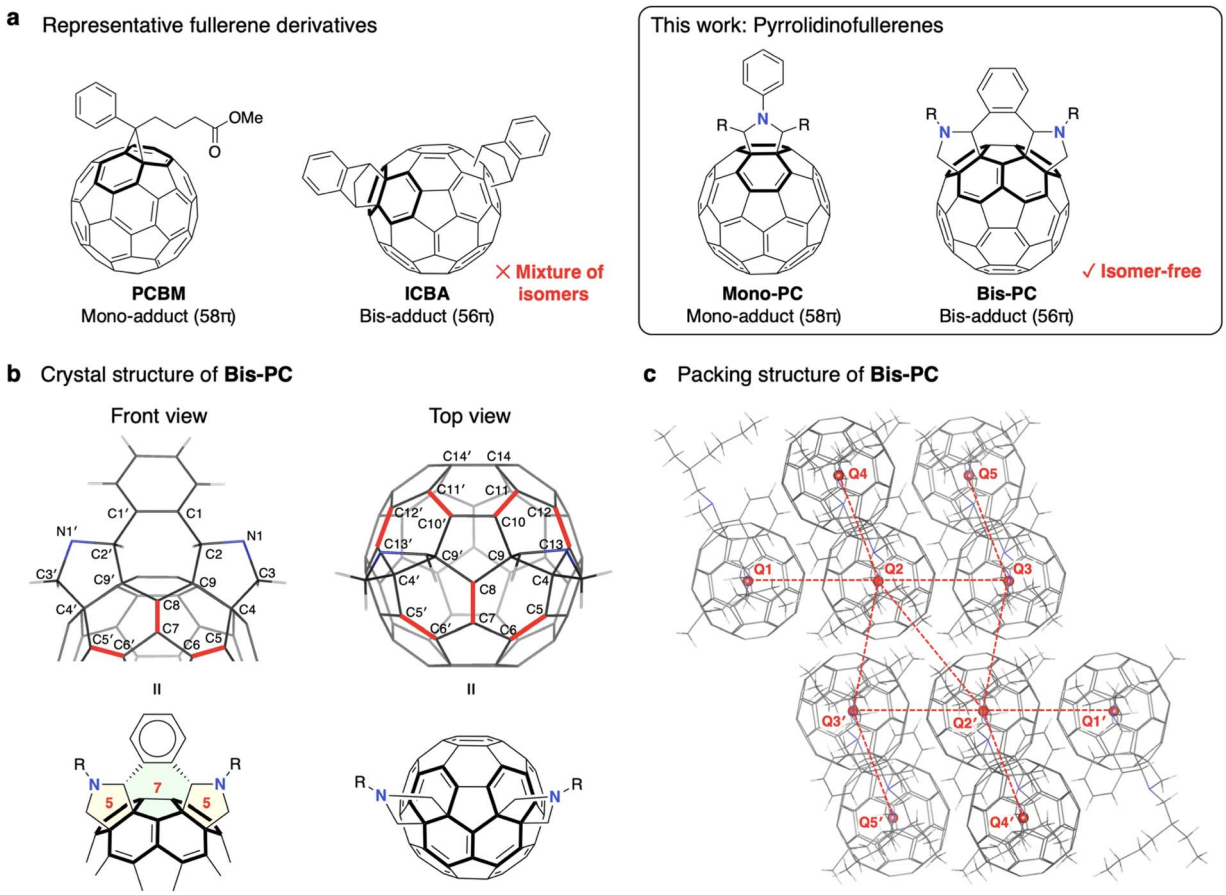

Fig. 1 Structures of pyrrolidinofullerenes in this study. (a) Chemical structures of representative fullerene derivatives, **PCBM** and **ICBA**, and mono and bis(pyrrolidino)fullerenes, **Mono-PC** and **Bis-PC**. (b) Single crystal structure of **Bis-PC**. Selected bond lengths (Å): C1′–C1, 1.424(6); C1–C2, 1.534(7); C2–C9, 1.559(6); C2–N1, 1.469(6); N1–C3, 1.475(6); C3–C4, 1.550(7); C4–C9, 1.597(7); C4–C5, 1.527(7); C5–C6, 1.354(7); C6–C7, 1.479(6); C7–C8, 1.350(6); C8–C9, 1.483(6); C9–C10, 1.517(7); C10–C11, 1.375(7); C11–C12, 1.480(7); C12–C13, 1.368(7); C13–C4, 1.539(7); C10′–C10, 1.417(6); C10–C11, 1.375(7); C14′–C14, 1.400(7). (c) Packing structure of **Bis-PC**. Selected centroid–centroid distances (CCDs) between fullerene cages (nm): Q1–Q2, 0.984; Q2–Q3, 0.984; Q2–Q4, 1.296; Q2–Q3′, 0.995; Q2–Q2, 1.014.

They succeeded in isolating four regioisomers and found that pure isomers resulted in solar cells with higher performance than the mixture. The same group later reported that the selective synthesis of a single isomer could be achieved by temporarily adding bulky substituents to control the steric hindrance during the introduction of ethylmalonate.[43] Using a supramolecular complex is another powerful method to access single-isomer bisadducts of fullerenes.[44–46] Recently, our group successfully used a single-isomer open-cage bis[60]fulleroid in Sn PSCs.[47]

Herein, we report phenylene-bridged bis(pyrrolidino) fullerene,[48,49] **Bis-PC**, for use as an ETM in Sn PSCs (Fig. 1a). The molecular design features geometrical restrictions to induce the preferential formation of the *cis*-2 bisadduct. Mono(pyrrolidino) fullerene, **Mono-PC**, was synthesized as a reference compound to investigate how the energy level alignment affects the device performance. The effect of methylammonium (MA) incorporation into the A-site of $PEA_{0.15}FA_{0.85}SnI_3$ was also studied. The combined use of the **Bis-PC** ETM and $PEA_{0.15}(FA_{0.87}MA_{0.13})_{0.85}SnI_3$ perovskite composition resulted in 3000 h shelf-stable devices with a maximum PCE of 12.3% and a V_{OC} of 0.86 V (V_{OC} loss of 0.51 V).

Results and discussion

Synthesis and characterization

The target bis(pyrrolidino)fullerene, **Bis-PC**, was synthesized in one step from C_{60} by the 1,3-dipolar cycloaddition of an ylide formed by the reaction of *o*-phthalaldehyde and *N*-(2-ethylhexyl) glycine.[48,49] The 2-ethylhexyl group was introduced to make the compound soluble enough to use as a solution-processable ETM (>20 mg mL^{-1} in chlorobenzene). The mono(pyrrolidino) fullerene, **Mono-PC**, was synthesized by the reaction of C_{60} with heptanal and 2-(phenylamino)octanoic acid.[50] These compounds were characterized by nuclear magnetic resonance (NMR), mass spectrometry (MS), and single-crystal X-ray structure analysis.

Single crystals of **Bis-PC** were grown by slowly cooling the solution of **Bis-PC** in chlorobenzene from 70 °C to room temperature. The front and top views of the crystal structure are shown in Fig. 1b. The five-membered pyrrolidine rings adopt an envelope form, whereas the central seven-membered ring is in a twist-chair form. The fused benzene ring is bent backward towards the fullerene, with a 108° dihedral angle between the

pyrrolidine rings and the benzene. As for the bond lengths, C5–C6 [1.354(7) Å] and C7–C8 [1.350(6) Å] are much shorter than C4–C5 [1.527(7) Å], C6–C7 [1.479(6) Å], C8–C9 [1.483(6) Å], and C9–C4 [1.597(7) Å]. This suggests that the diene character emerged after pyrrolidine was added to the C9–C4 bonds. Similarly, a significant bond alternation was observed where the bonds shown in red lines have a strong double bond character. These trends of the bond lengths are comparable to those of similar fullerene bisadducts.[51]

The molecular packing structure of **Bis-PC** is shown in Fig. 1c and S1.† It is reported that electrons can be transported efficiently between fullerene cages when the centroid–centroid distance (CCD) is about 1 nm.[52,53] In our compound, one fullerene molecule (*e.g.* Q2) is surrounded by five carbon cages (*e.g.* Q1, Q3, Q4, Q2′, and Q3′), with CCDs of Q1–Q2 [0.984 nm], Q2–Q3 [0.984 nm], Q2–Q4 [1.296 nm], Q2–Q3′ [0.995 nm], and Q2–Q2′ [1.014 nm]. This results in an average CCD of 1.05 nm, indicating that efficient electron transport is feasible within this structure.

Basic properties

The electrochemical properties of the fullerenes were evaluated by cyclic voltammetry (CV) in *o*-dichlorobenzene (ODCB) (Fig. 2a). Both **Mono-PC** and **Bis-PC** exhibit two reversible reduction waves. The first reduction potential of **Bis-PC** ($E_{1/2}$ = −1.41 V *vs.* Fc/Fc$^+$) is negatively shifted compared to that of **Mono-PC** ($E_{1/2}$ = −1.21 V) by 0.20 V, suggesting that the electron-accepting ability of **Bis-PC** is weaker than that of **Mono-PC**. The LUMO energy levels estimated from the onset of the first reduction potentials[54] are −3.96 and −3.76 eV for **Mono-PC** and **Bis-PC**, comparable to those of **PCBM** and **ICBA**, respectively (Fig. 2b). The tendency of the electronic structures of the fullerene derivatives was consistent with the density functional theory (DFT) calculations (Fig. S2†). The LUMO energy levels of fullerenes were also evaluated using low-energy inverse photoelectron spectroscopy (LEIPS).[55–57] To ensure the reliability of the data, the LEIPS measurements were conducted for 5, 10, and 15 nm-thick films with two wavelengths of photon detection (260 and 285 nm), and the average value was calculated (raw data in Fig. S3 and S4,† and histogram in Fig. S5†). The average LUMO energies were determined to be −3.59 ± 0.02, −3.52 ± 0.14, −3.73 ± 0.02, and −3.59 ± 0.04 eV for **Mono-PC**, **Bis-PC**, **PCBM**, and **ICBA**, respectively (Fig. 2b). These values for **PCBM** and **ICBA** are in good agreement with the previously measured values.[58,59] Although the absolute values are influenced by crystallinity and orientation of molecular dipoles,[60,61] the general trend of the bisadduct having higher LUMO levels than the monoadduct was confirmed, consistent with the result of cyclic voltammetry.

The crystallinity and morphology of the films were evaluated by two-dimensional grazing-incidence X-ray diffraction (2D-GIXD) and atomic force microscopy (AFM) techniques. Thin

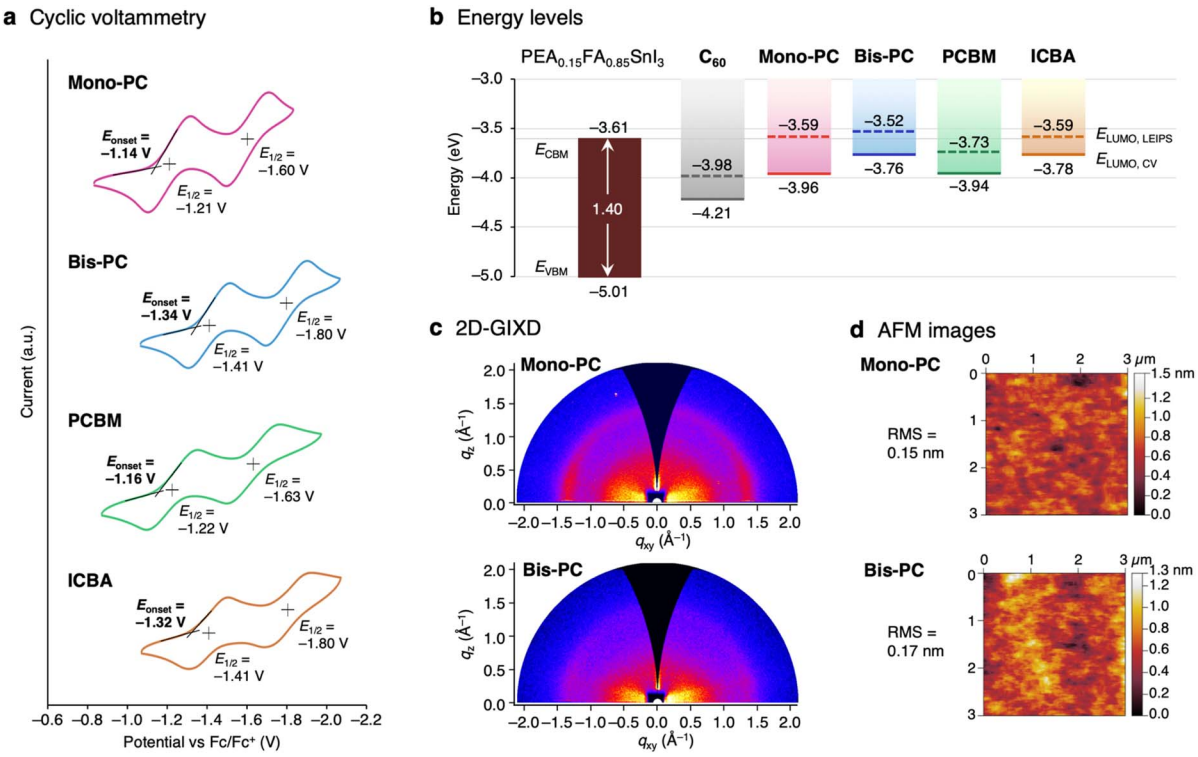

Fig. 2 Basic properties of pyrrolidinofullerene derivatives. (a) Cyclic voltammograms of **Mono-PC**, **Bis-PC**, **PCBM**, and **ICBA** recorded in *o*-dichlorobenzene at a scan rate of 100 mV s^{-1} using *n*-Bu_4NPF_6 as the supporting electrolyte. (b) Energy level diagrams of the tin perovskite $PEA_{0.15}FA_{0.85}SnI_3$ and the fullerene derivatives. The E_{LUMO} values for C_{60} were taken from the previous reports.[19,58] (c) Two-dimensional grazing-incidence X-ray diffraction (2D-GIXD) and (d) atomic force microscope (AFM) images for the *ca.* 50 nm thick thin films of **Mono-PC** and **Bis-PC** fabricated on Si substrates.

films were prepared on Si substrates by spin-coating, using a 20 mg mL^{-1} solution of fullerene derivatives in chlorobenzene. The thicknesses of **Mono-PC** and **Bis-PC** films were estimated by ellipsometry to be 47.2 ± 0.1 and 49.6 ± 0.1 nm, respectively (Table S1†). The 2D-GIXD patterns of **Mono-PC** and **Bis-PC** films show no obvious Bragg diffraction, suggesting that these films are essentially amorphous (Fig. 2c). The AFM images of **Mono-PC** and **Bis-PC** films exhibit smooth surfaces with a root-mean-square (RMS) roughness of less than 0.2 nm (Fig. 2d). As reported in our previous study,[62] amorphous, smooth films are ideal for ETMs to block holes completely and to prevent current leakage.

Device fabrication: comparison of ETMs

A quasi-2D/3D perovskite, $PEA_{0.15}FA_{0.85}SnI_3$, was used as the light-absorbing layer for evaluating the fullerene derivatives as ETMs in inverted-type solar cell devices. The device structure is glass/ITO/PEDOT:PSS/$PEA_{0.15}FA_{0.85}SnI_3$/fullerenes/bathocuproine (BCP)/Ag (Fig. 3a). The current–voltage (*J–V*) curves of the devices are shown in Fig. 3b, and device parameters are summarized in Table 1. The device using **Mono-PC** showed a PCE of 6.63% with a J_{SC} of 18.3 mA cm^{-2}, a V_{OC} of 0.54 V, and a FF of 0.67 (forward scan), which is an overall higher performance than the **PCBM**-based device (PCE = 4.78%). The **Bis-PC**-based device, meanwhile, exhibited a PCE of 9.70% with a V_{OC} of 0.78 V. The V_{OC} of the **Bis-PC**-based device increased from the **Mono-PC** or **PCBM**-based device and is comparable to that of the **ICBA**-based device (V_{OC} = 0.77 V). The improved V_{OC} of the **Bis-PC**-based device can be ascribed to the reduced energy offset between E_{LUMO} of the ETM and E_{CBM} of perovskite; 0.15 eV for **Bis-PC** compared to 0.35 eV for **Mono-PC**. The integrated J_{SC} from the external quantum efficiency (EQE) spectrum was confirmed to be similar to the values obtained from the *J–V* curves (Fig. S6†). The statistical distribution from 12 devices is summarized in Fig. 3c, revealing that the overall performance in terms of V_{OC} is **PCBM** < **Mono-PC** < **Bis-PC** ≒ **ICBA**. The **ICBA**-based device showed higher PCE (10.4 ± 0.5%) than **Bis-PC** (9.1 ± 0.7%) due to the higher fill factor (0.72 ± 0.02 for **ICBA** and 0.64 ± 0.02 for **Bis-PC**). The low fill factor of **Bis-PC**-based devices is ascribed to the moderate electron mobility of **Bis-PC** (2.6×10^{-5} cm^2 V^{-1} s^{-1}) estimated by the space-charge limited current (SCLC) method (Fig. S7†). Fig. 3d represents the long-term stability of the devices stored under a nitrogen atmosphere. The device efficiency with mixed-isomer **ICBA** drops to 35% after storage for 1000 hours. In contrast, the device with single-isomer **Bis-PC** exhibited high stability, retaining its initial efficiency for over 3000 hours. The higher thermal stability of **Bis-PC** (T_{d5} = 361 °C) in thermogravimetric analysis (TGA) compared to **ICBA** (250 °C, Fig. S8†), and the higher amorphous stability of **Bis-PC** films up to 180 °C (Fig. S9†) are likely related to the superior shelf stability of **Bis-PC**-based solar cell devices.

Device fabrication: perovskite composition engineering

Encouraged by the high stability of the **Bis-PC**-based device, we envisioned that the device efficiency could be further increased by optimizing the perovskite composition. From our previous studies on FA/MA mixed tin perovskites,[23,63] solar cell devices were fabricated with a perovskite composition of $PEA_{0.15}(FA_{1-x}MA_x)_{0.85}SnI_3$ (x = 0.00, 0.13, 0.25, 0.50, and 1.00), where FA

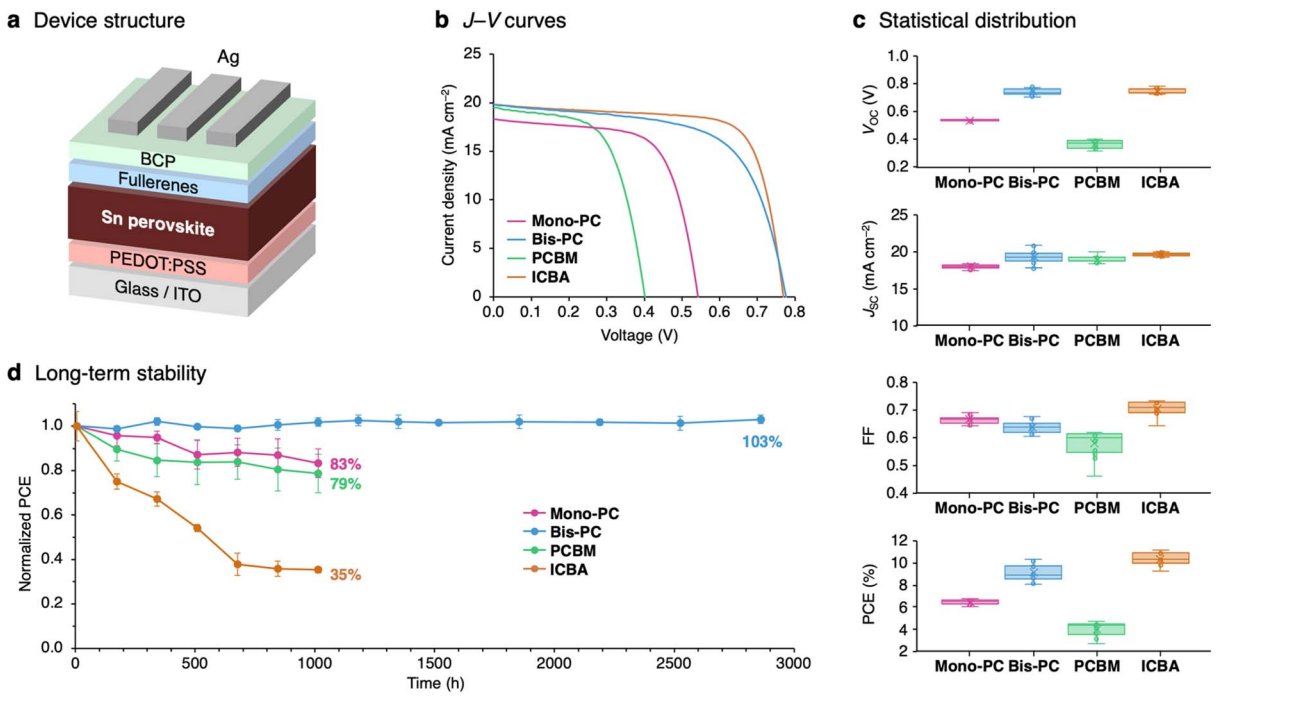

Fig. 3 Comparison of fullerene-based electron-transporting materials. (a) Device structure and (b) current–voltage (*J–V*) curves of tin perovskite solar cells using different electron-transporting materials. (c) Statistical distribution of photovoltaic parameters and (d) long-term stability under nitrogen conditions.

Table 1 Photovoltaic parameters of tin perovskite solar cells using fullerene-based electron-transporting materials (ETMs)

ETM	J_{SC}[a] (mA cm^{-2})	V_{OC}[a] (V)	FF[a]	PCE[a] (%)
Mono-PC	18.32 (18.2 ± 0.2)	0.54 (0.54 ± 0.00)	0.67 (0.66 ± 0.01)	6.63 (6.4 ± 0.2)
Bis-PC	19.85 (19.7 ± 0.6)	0.78 (0.74 ± 0.02)	0.63 (0.63 ± 0.01)	9.70 (9.1 ± 0.7)
PCBM	19.52 (19.2 ± 0.4)	0.40 (0.37 ± 0.02)	0.61 (0.59 ± 0.03)	4.78 (4.2 ± 0.5)
ICBA	19.85 (19.7 ± 0.2)	0.77 (0.75 ± 0.02)	0.73 (0.71 ± 0.02)	11.18 (10.4 ± 0.5)

[a] The average and standard deviation values for 12 devices are given in parentheses.

is replaced with different amounts of MA (cross-sectional and surface scanning-electron microscopy images shown in Fig. S10 and S11,† respectively). The systematic mixing of FA and MA was confirmed using X-ray diffraction (XRD) spectra, showing the linear decrease of the interplanar spacing (d_{100}) with respect to the MA ratio (Fig. S12†). The *J*–*V* curves show that both J_{SC} and V_{OC} were improved by incorporating a small amount of MA ($x = 0.13$, Fig. 4a). The highest PCE of 12.27% was obtained for this fraction of MA, with a J_{SC} of 21.69 mA cm^{-2}, a V_{OC} of 0.86 V, and a FF of 0.66. Further addition of MA decreased the device efficiency, with PCEs of 11.57%, 9.35%, and 4.77% for $x = 0.25$, 0.50, and 1.00 composition, respectively (Fig. S13 and Table S2†). The IPCE spectra show an increase in the maximum EQE value from 68% for the FA-only ($x = 0.00$) device to 76% for the MA-incorporated ($x = 0.13$) device, as well as a slight shift of the onset to a longer wavelength (Fig. 4b). The MA-incorporated ($x = 0.13$) device showed stable power output for 300 s under AM 1.5G illumination (Fig. S14†). The statistical distribution of the device parameters (Fig. 4c) clearly shows the increase of J_{SC}, V_{OC}, and PCE with the incorporation of MA ($x = 0.13$). The electrical impedance spectra of the MA-incorporated ($x = 0.13$) device show higher recombination resistance than the FA-only ($x = 0.00$) device (Fig. 4d for the spectra measured at 0.2 V bias, Fig. S15† for the full set of data), explaining the higher V_{OC} observed in the *J*–*V* curves.

The device performance was evaluated at various light intensities ranging from 1 sun to 0.01 sun (Fig. S16†). The light intensity dependence of V_{OC} is shown in Fig. S17a.† The estimated ideality factor of the MA-incorporated ($x = 0.13$) device ($n_{id} = 1.50$) is smaller than that of the FA-only ($x = 0.00$) device ($n_{id} = 1.57$), indicating the smaller effect of trap states.[64] The fill factor of the FA-only ($x = 0.00$) device is maximized at the light intensity of 5 mW cm^{-2} (0.05 sun), whereas that of the MA-incorporated ($x = 0.13$) device keeps increasing as the light intensity is reduced, showing the highest FF of 0.71 under the 1 mW cm^{-2} (0.01 sun) irradiation (Fig. S17c†). Encouraged by the generally good performance at low light intensity, device efficiency under indoor lighting conditions was evaluated using an 800 lux white LED (0.30 mW cm^{-2}, spectrum shown in Fig. S18b†). The MA-incorporated ($x = 0.13$) device showed

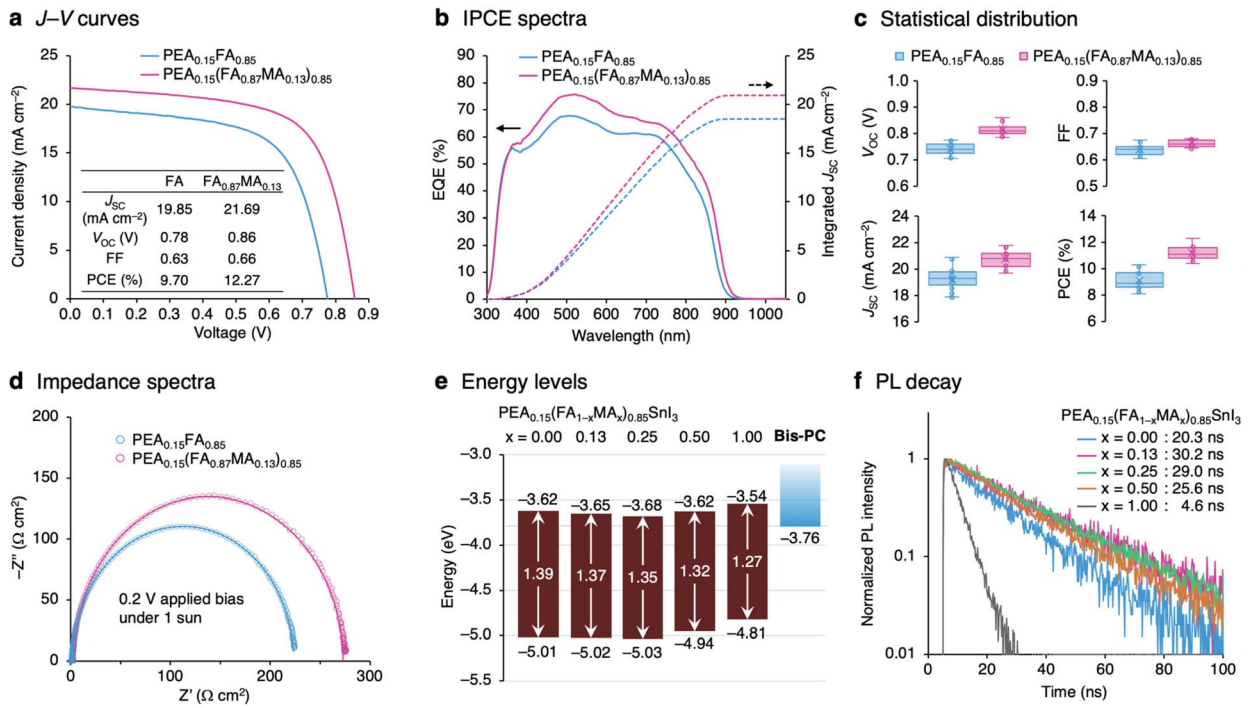

Fig. 4 Effect of MA incorporation on the device performance. (a) *J*–*V* curves and (b) EQE spectra of tin perovskite solar cells using perovskite compositions of $PEA_{0.15}FA_{0.85}SnI_3$ and $PEA_{0.15}(FA_{0.87}MA_{0.13})_{0.85}SnI_3$ with **Bis-PC** as the electron-transporting material. (c) Statistical distribution of photovoltaic parameters. (d) Electrical impedance spectra under 0.2 V applied bias and 1-sun illumination. (e) Energy level diagrams and (f) photoluminescence decay curves of $PEA_{0.15}(FA_{1-x}MA_x)_{0.85}SnI_3$ ($x = 0.00$, 0.13, 0.25, 0.50, and 1.00) films.

a PCE of 13.8% with a J_{SC} of 96.1 μA cm^{-2}, a V_{OC} of 0.61 V, and a FF of 0.70, which is higher than that of the FA-only ($x = 0.00$) device with a PCE of 9.9% (Fig. S18a†).

The MA-incorporated ($x = 0.13$) device also shows high long-term stability comparable to the FA-only system ($x = 0.00$), retaining its initial efficiency for 3000 hours (Fig. S19†). Thermostability was evaluated by repeating the process of heating the devices for one hour and measuring the *J–V* characteristics, increasing the temperature by 10 °C after each cycle (Fig. S20†). Both FA-only ($x = 0.00$) and MA-incorporated ($x = 0.13$) devices retained 90% of their initial performances after heating up to 90 °C.

To gain insight into how composition engineering improves device performance, the energy levels and photoluminescence (PL) properties of perovskite films were evaluated. Fig. S21a† represents the photoemission yield spectroscopy (PYS) spectra of $PEA_{0.15}(FA_{1-x}MA_x)_{0.85}SnI_3$ films fabricated on glass/ITO/PEDOT:PSS substrates. Ionization energies (IEs) determined from the onset of PYS spectra were found to be almost constant until $x = 0.25$ (IE = 5.01, 5.02, and 5.03 eV for $x = 0.00$, 0.13, and 0.25 composition, respectively), and then became smaller, 4.94 eV and 4.81 eV for $x = 0.50$ and 1.00, respectively. The PL spectra of $PEA_{0.15}(FA_{1-x}MA_x)_{0.85}SnI_3$ films are shown in Fig. S21b.† Increasing the fraction of MA caused the PL peak position to gradually shift to lower energy, from 1.39 eV for $x =$ 0.00 to 1.27 eV for $x = 1.00$. The shift mirrors the change in the bandgap caused by the decrease in the average A-site radius. By adding the bandgap energy (E_g) estimated from the PL peak position to the valence band maximum energy ($E_{VBM} = -IE$), the conduction band minimum ($E_{CBM} = E_{VBM} + E_g$) was estimated (Fig. 4e). It was found that compared to the FA-only ($x = 0.00$; $E_{CBM} = -3.62$ eV) and MA-only ($x = 1.00$; $E_{CBM} = -3.54$ eV) systems, mixing two cations causes E_{CBM} to become deeper ($E_{CBM} = -3.65$, -3.68, and -3.62 eV for $x = 0.13$, 0.25, and 0.50, respectively). Interestingly, a strong correlation was observed between the conduction band minimum energies and the PL lifetimes. The mixed-cation systems show longer PL lifetimes (30.2 ns, 29.0 ns, and 25.6 ns for $x = 0.13$, 0.25, and 0.50) compared to FA-only ($x = 0.00$; 20.3 ns) and MA-only ($x = 1.00$; 4.6 ns) systems (Fig. 4f). Long PL lifetimes observed in the mixed-cation compositions with low E_{CBM} suggest a reduction in internal deep trap states and suppressed nonradiative recombination. Fig. S22† shows the relationship between the V_{OC} loss from the bandgap ($E_g - qV_{OC}$) and the energy level offset ($E_{LUMO} - E_{CB}$). The strong correlation of these two parameters suggests that the use of the ETM with high-lying LUMO energy and the selection of perovskite composition with low conduction band energy are important to minimize the voltage loss.

Conclusions

In summary, we synthesized a single-isomer fullerene bisadduct, phenylene-bridged bis(pyrrolidino)fullerene (**Bis-PC**) as well as mono(pyrrolidino)fullerene (**Mono-PC**), as ETMs in tin halide perovskite solar cells. **Bis-PC** with high-lying LUMO levels gave a higher V_{OC} when used in $PEA_{0.15}FA_{0.85}SnI_3$-based solar cell devices. More importantly, the device with single-isomer **Bis-PC** shows higher stability compared to that with mixed-isomer **ICBA**. The FA/MA-mixed $PEA_{0.15}(FA_{1-x}MA_x)_{0.85}SnI_3$ system was also studied, providing a clear correlation between the lower E_{CBM} of the perovskite composition, the longer PL lifetime, and the lower V_{OC} loss in the solar cell device. Specifically, the device using the **Bis-PC** ETM and $PEA_{0.15}(FA_{0.87}MA_{0.13})_{0.85}SnI_3$ perovskite composition exhibited a maximum PCE of 12.3% with a V_{OC} of 0.86 V (V_{OC} loss of 0.51 V). Our findings offer valuable insights for further improving the efficiency and stability of tin halide perovskite solar cells.

Data availability

Crystallographic data for **Bis-PC** have been deposited with the Cambridge Crystallographic Data Center as supplementary publication no. CCDC-2369060. These data can be obtained free of charge from the Cambridge Crystallographic Data Centre *via* https://www.ccdc.cam.ac.uk/data_request/cif.

Author contributions

T. Nak. conceived the idea. T. Nak. and A. W. supervised the project. T. Nag. and Y. M. carried out the synthesis and characterization of the materials. T. Nak. conducted the X-ray structure analysis, XRD and AFM measurements, and device fabrication/characterization. Y. M. conducted the CV measurements. M. M. and H. Y. carried out the LEIPS measurements. R. M. conducted the impedance measurement. T. Nak. conducted the PL measurements with the help of T. Y. and Y. K. T. Nak. wrote the original draft of the manuscript. M. A. T., R. M., and A. W. edited the manuscript. All authors commented on the manuscript.

Conflicts of interest

A. W. is co-founder and CSO of EneCoat Technologies, Co., Ltd

Acknowledgements

This work was partially supported by JST–Mirai (JPMJMI22E2) programs, NEDO (JPNP20015), NEDO-GI (JPNP21016), International Collaborative Research Program of ICR, Kyoto University, Grant-in-Aid for Scientific Research (A) (JP24H00481), and Grant-in-Aid for Scientific Research (B) (JP24K01571 and JP24K01607). Additional funding was provided by research grants from the Sumitomo Foundation, the Nippon Shokubai Award in Synthetic Organic Chemistry, Japan, and the JACI Prize for Encouraging Young Researcher. We thank Prof. Takeshi Hasegawa, Dr Nobutaka Shioya, and Dr Noriko Kurose (ICR, Kyoto University) for XRD measurements. We also thank Prof. Kenichiro Itami, Dr Kazuma Amaike (RIKEN), and Dr Nobutaka Honma (Toyota Motor Corporation) for fruitful discussions.

Notes and references

1 M. A. Green, A. Ho-Baillie and H. J. Snaith, *Nat. Photonics*, 2014, **8**, 506–514.
2 Y. Rong, Y. Hu, A. Mei, H. Tan, M. I. Saidaminov, S. Il Seok, M. D. McGehee, E. H. Sargent and H. Han, *Science*, 2018, **361**, eaat8235.
3 H. J. Snaith, *Nat. Mater.*, 2018, **17**, 372–376.
4 A. K. Jena, A. Kulkarni and T. Miyasaka, *Chem. Rev.*, 2019, **119**, 3036–3103.
5 Best Research Cell Efficiencies Chart, **https://www.nrel.gov/pv/assets/pdfs/best-research-cell-efficiencies.pdf**, Accessed 11th December 2024.
6 J. Li, H. L. Cao, W. Bin Jiao, Q. Wang, M. Wei, I. Cantone, J. Lü and A. Abate, *Nat. Commun.*, 2020, **11**, 310.
7 M. Ren, X. Qian, Y. Chen, T. Wang and Y. Zhao, *J. Hazard. Mater.*, 2022, **426**, 127848.
8 M. Konstantakou and T. Stergiopoulos, *J. Mater. Chem. A*, 2017, **5**, 11518–11549.
9 W. Ke and M. G. Kanatzidis, *Nat. Commun.*, 2019, **10**, 965.
10 W. Ke, C. C. Stoumpos and M. G. Kanatzidis, *Adv. Mater.*, 2019, **31**, 1803230.
11 J. Cao and F. Yan, *Energy Environ. Sci.*, 2021, **14**, 1286–1325.
12 L. Xu, X. Feng, W. Jia, W. Lv, A. Mei, Y. Zhou, Q. Zhang, R. Chen and W. Huang, *Energy Environ. Sci.*, 2021, **14**, 4292–4317.
13 T. Nakamura, T. Handa, R. Murdey, Y. Kanemitsu and A. Wakamiya, *ACS Appl. Electron. Mater.*, 2020, **2**, 3794–3804.
14 E. Aktas, N. Rajamanickam, J. Pascual, S. Hu, M. H. Aldamasy, D. Di Girolamo, W. Li, G. Nasti, E. Martínez-Ferrero, A. Wakamiya, E. Palomares and A. Abate, *Commun. Mater.*, 2022, **3**, 104.
15 S. Hu, J. A. Smith, H. J. Snaith and A. Wakamiya, *Precis. Chem.*, 2023, **1**, 69–82.
16 W. Shockley and H. J. Queisser, *J. Appl. Phys.*, 1961, **32**, 510–519.
17 S. Rühle, *Sol. Energy*, 2016, **130**, 139–147.
18 F. Gu, S. Ye, Z. Zhao, H. Rao, Z. Liu, Z. Bian and C. Huang, *Sol. RRL*, 2018, **2**, 1800136.
19 T. Nakamura, S. Yakumaru, M. A. Truong, K. Kim, J. Liu, S. Hu, K. Otsuka, R. Hashimoto, R. Murdey, T. Sasamori, H. Do Kim, H. Ohkita, T. Handa, Y. Kanemitsu and A. Wakamiya, *Nat. Commun.*, 2020, **11**, 3008.
20 J. Sanchez-Diaz, R. S. Sánchez, S. Masi, M. Krecmarová, A. O. Alvarez, E. M. Barea, J. Rodriguez-Romero, V. S. Chirvony, J. F. Sánchez-Royo, J. P. Martinez-Pastor and I. Mora-Seró, *Joule*, 2022, **6**, 861–883.
21 T. Nakamura, Y. Kondo, N. Ohashi, C. Sakamoto, A. Hasegawa, S. Hu, M. A. Truong, R. Murdey, Y. Kanemitsu and A. Wakamiya, *Bull. Chem. Soc. Jpn.*, 2024, **97**, uoad025.
22 S. Shao, J. Liu, G. Portale, H. H. Fang, G. R. Blake, G. H. ten Brink, L. J. A. Koster and M. A. Loi, *Adv. Energy Mater.*, 2018, **8**, 1702019.
23 T. Nakamura, K. Otsuka, S. Hu, R. Hashimoto, T. Morishita, T. Handa, T. Yamada, M. A. Truong, R. Murdey, Y. Kanemitsu and A. Wakamiya, *ACS Appl. Energy Mater.*, 2022, **5**, 14789–14798.
24 E. Nakanishi, R. Nishikubo, F. Ishiwari, T. Nakamura, A. Wakamiya and A. Saeki, *ACS Mater. Lett.*, 2022, **4**, 1124–1131.
25 C. Kuan, T. Liao, S. Narra, Y. Tsai, J. Lin, G. Chen and E. W. Diau, *J. Phys. Chem. Lett.*, 2024, **15**, 7763–7769.
26 S. Hu, J. Pascual, W. Liu, T. Funasaki, M. A. Truong, S. Hira, R. Hashimoto, T. Morishita, K. Nakano, K. Tajima, R. Murdey, T. Nakamura and A. Wakamiya, *ACS Appl. Mater. Interfaces*, 2022, **14**, 56290–56297.
27 L. Wang, Q. Miao, D. Wang, M. Chen, H. Bi, J. Liu, A. K. Baranwal, G. Kapil, Y. Sanehira, T. Kitamura, T. Ma, Z. Zhang, Q. Shen and S. Hayase, *Angew. Chem., Int. Ed.*, 2023, **62**, e202307228.
28 J. Chen, J. Luo, E. Hou, P. Song, Y. Li, C. Sun, W. Feng, S. Cheng, H. Zhang, L. Xie, C. Tian and Z. Wei, *Nat. Photonics*, 2024, **18**, 464–470.
29 Y. Shi, Z. Zhu, D. Miao, Y. Ding and Q. Mi, *ACS Energy Lett.*, 2024, **9**, 1895–1897.
30 S. Tao, I. Schmidt, G. Brocks, J. Jiang, I. Tranca, K. Meerholz and S. Olthof, *Nat. Commun.*, 2019, **10**, 2560.
31 T. Umeyama and H. Imahori, *Acc. Chem. Res.*, 2019, **52**, 2046–2055.
32 Z. Xing, S. H. Li and S. Yang, *Small Struct.*, 2022, **3**, 2200012.
33 X. Jiang, F. Wang, Q. Wei, H. Li, Y. Shang, W. Zhou, C. Wang, P. Cheng, Q. Chen, L. Chen and Z. Ning, *Nat. Commun.*, 2020, **11**, 1245.
34 X. Jiang, H. Li, Q. Zhou, Q. Wei, M. Wei, L. Jiang, Z. Wang, Z. Peng, F. Wang, Z. Zang, K. Xu, Y. Hou, S. Teale, W. Zhou, R. Si, X. Gao, E. H. Sargent and Z. Ning, *J. Am. Chem. Soc.*, 2021, **143**, 10970–10976.
35 B. Bin Yu, Z. Chen, Y. Zhu, Y. Wang, B. Han, G. Chen, X. Zhang, Z. Du and Z. He, *Adv. Mater.*, 2021, **33**, 2102055.
36 T. Wang, H. L. Loi, J. Cao, Z. Qin, Z. Guan, Y. Xu, H. Cheng, M. G. Li, C. S. Lee, X. Lu and F. Yan, *Adv. Sci.*, 2022, **9**, 2200242.
37 Z. Zhu, X. Jiang, D. Yu, N. Yu, Z. Ning and Q. Mi, *ACS Energy Lett.*, 2022, **7**, 2079–2083.
38 W. Liu, S. Hu, J. Pascual, K. Nakano, R. Murdey, K. Tajima and A. Wakamiya, *ACS Appl. Mater. Interfaces*, 2023, **15**, 32487–32495.
39 Y. He, H. Y. Chen, J. Hou and Y. Li, *J. Am. Chem. Soc.*, 2010, **132**, 1377–1382.
40 T. Cao, N. Chen, G. Liu, Y. Wan, J. D. Perea, Y. Xia, Z. Wang, B. Song, N. Li, X. Li, Y. Zhou, C. J. Brabec and Y. Li, *J. Mater. Chem. A*, 2017, **5**, 10206–10219.
41 Y. Lin, B. Chen, F. Zhao, X. Zheng, Y. Deng, Y. Shao, Y. Fang, Y. Bai, C. Wang and J. Huang, *Adv. Mater.*, 2017, **29**, 1700607.
42 C. Sun, P. Yang, Z. Nan, C. Tian, Y. Cai, J. Chen, F. Qi, H. Tian, L. Xie, L. Meng and Z. Wei, *Adv. Mater.*, 2023, **35**, 2205603.
43 P. Yang, C. Sun, X. Fu, S. Cheng, J. Chen, H. Zhang, Z. A. Nan, J. Yang, X. J. Zhao, L. Q. Xie, L. Meng, C. Tian and Z. Wei, *J. Am. Chem. Soc.*, 2024, **146**, 2494–2502.

44 C. Fuertes-Espinosa, C. García-Simón, M. Pujals, M. Garcia-Borràs, L. Gómez, T. Parella, J. Juanhuix, I. Imaz, D. Maspoch, M. Costas and X. Ribas, *Chem*, 2020, **6**, 169–186.
45 V. Leonhardt, S. Fimmel, A. M. Krause and F. Beuerle, *Chem. Sci.*, 2020, **11**, 8409–8415.
46 E. Ubasart, O. Borodin, C. Fuertes-Espinosa, Y. Xu, C. García-Simón, L. Gómez, J. Juanhuix, F. Gándara, I. Imaz, D. Maspoch, M. von Delius and X. Ribas, *Nat. Chem.*, 2021, **13**, 420–427.
47 W. Liu, G. Huang, C. Y. Chen, T. Tan, H. Fuyuki, S. Hu, T. Nakamura, M. A. Truong, R. Murdey, Y. Hashikawa, Y. Murata and A. Wakamiya, *Chem. Commun.*, 2024, **60**, 2172–2175.
48 M. Izquierdo, M. R. Cerõn, N. Alegret, A. J. Metta-Magaña, A. Rodríguez-Fortea, J. M. Poblet and L. Echegoyen, *Angew. Chem., Int. Ed.*, 2013, **52**, 12928–12931.
49 A. V. Mumyatov, F. A. Prudnov, D. K. Sagdullina, I. V. Martynov, L. N. Inasaridze, A. V. Chernyak, A. V. Maskaev, I. E. Kuznetsov, A. V. Akkuratov and P. A. Troshin, *Synth. Met.*, 2021, **271**, 116632.
50 H. R. Le Sueur, *J. Chem. Soc., Trans.*, 1910, **97**, 2433–2441.
51 J. Nierengarten, V. Gramlich, F. Cardullo and F. Diederich, *Angew Chem. Int. Ed. Engl.*, 1996, **35**, 2101–2103.
52 H. Bässler, *Phys. Status Solidi B*, 1993, **175**, 15–56.
53 X. Sun, L. Y. Ji, W. W. Chen, X. Guo, H. H. Wang, M. Lei, Q. Wang and Y. F. Li, *J. Mater. Chem. A*, 2017, **5**, 20720–20728.
54 C. M. Cardona, W. Li, A. E. Kaifer, D. Stockdale and G. C. Bazan, *Adv. Mater.*, 2011, **23**, 2367–2371.
55 H. Yoshida, *Chem. Phys. Lett.*, 2012, **539–540**, 180–185.
56 H. Yoshida, *Anal. Bioanal. Chem.*, 2014, **406**, 2231–2237.
57 H. Yoshida, *J. Electron Spectros. Relat. Phenomena*, 2015, **204**, 116–124.
58 H. Yoshida, *J. Phys. Chem. C*, 2014, **118**, 24377–24382.
59 A. Sugie, K. Nakano, K. Tajima, I. Osaka and H. Yoshida, *J. Phys. Chem. Lett.*, 2023, **14**, 11412–11420.
60 Y. Zhong, S. Izawa, K. Hashimoto, K. Tajima, T. Koganezawa and H. Yoshida, *J. Phys. Chem. C*, 2015, **119**, 23–28.
61 K. Akaike, T. Kumai, K. Nakano, S. Abdullah, S. Ouchi, Y. Uemura, Y. Ito, A. Onishi, H. Yoshida, K. Tajima and K. Kanai, *Chem. Mater.*, 2018, **30**, 8233–8243.
62 T. Nakamura, N. Shioya, T. Shimoaka, R. Nishikubo, T. Hasegawa, A. Saeki, Y. Murata, R. Murdey and A. Wakamiya, *Chem. Mater.*, 2019, **31**, 1729–1737.
63 J. Liu, M. Ozaki, S. Yakumaru, T. Handa, R. Nishikubo, Y. Kanemitsu, A. Saeki, Y. Murata, R. Murdey and A. Wakamiya, *Angew. Chem., Int. Ed.*, 2018, **57**, 13221–13225.
64 S. R. Cowan, A. Roy and A. J. Heeger, *Phys. Rev. B*, 2010, **82**, 245207.